Supplementary Information

Inverse 'Intra-Lattice' Charge Transfer in Nickel-Molybdenum Dual Electrocatalysts Regulated by Under-coordinating the Molybdenum Center

Sahanaz Parvin,[1] Neha Bothra,[2] Supriti Dutta,[2] Mamoni Maji,[1] Maglu Mura,[1] Ashwani Kumar,[1] Dhirendra K. Chaudhary,[1,3] Parasmani Rajput,[4] Manvendra Kumar,[5] Swapan K. Pati,[2] and Sayan Bhattacharyya[1,*]

[1]*Department of Chemical Sciences and Centre for Advanced Functional Materials, Indian Institute of Science Education and Research (IISER) Kolkata, Mohanpur - 741246, India*
[2]*Theoretical Sciences Unit, School of Advanced Materials, Jawaharlal Nehru Centre for Advanced Scientific Research, Bangalore 560064, India*
[3]*Centre for Renewable Energy, Prof. Rajendra Singh (Rajju Bhaiya) Institute of Physical Sciences for Study and Research, V. B. S. Purvanchal University, Jaunpur – 222003, India*
[4]*Beamline Development and Application Section, Bhabha Atomic Research Center, Trombay, Mumbai-400085, India*
[5]*Department of Physics, Institute of Science, Shri Vaishnav Vidyapeeth Viswavidyalaya, Indore, 453111, India*
*Email for correspondence: sayanb@iiserkol.ac.in

Table S1. The 2θ values of the reflections obtained from the XRD patterns of the samples, compared with the standard patterns from crystallographic open database (COD).

Standards/Samples	Plane	2θ (º)
Cu [COD ID 9012043]	(111)	43.3
	(200)	50.6
	(220)	74.3
Ni [COD ID 2100649]	(111)	44.7
	(200)	51.9
	(220)	76.6
Mo [COD ID 1534907]	(111)	38.8
	(200)	45.1
	(220)	65.5
	(311)	78.7
Ni$_{73}$Mo (Cu)	(111)	43.4
	(200)	50.6
	(220)	74.2
Ni$_{73}$Mo (Ni)	(111)	44.5
	(200)	51.8
	(220)	76.3
Ni-100-60m (Cu)	(111)	43.4
	(200)	50.6
	(220)	74.3
Ni-100-60m (Ni)	(111)	44.6
	(200)	51.9
	(220)	76.5
Mo-100-60m (Cu)	(111)	43.5
	(200)	50.7
	(220)	74.4
Mo-100-60m (Mo)*	(111)	39.2
β-Nickel Hydroxide [COD ID 9009112]	(100)	33.2
	(101)	38.6
NH-24	(100)	33
	(101)	38.4
NMH-24	(012)	34.3
	(015)	38.3
	(110)	59.6

*For Mo-100-60m, the intensity of (111) is plane is too low to be indexed in Figure 1c.
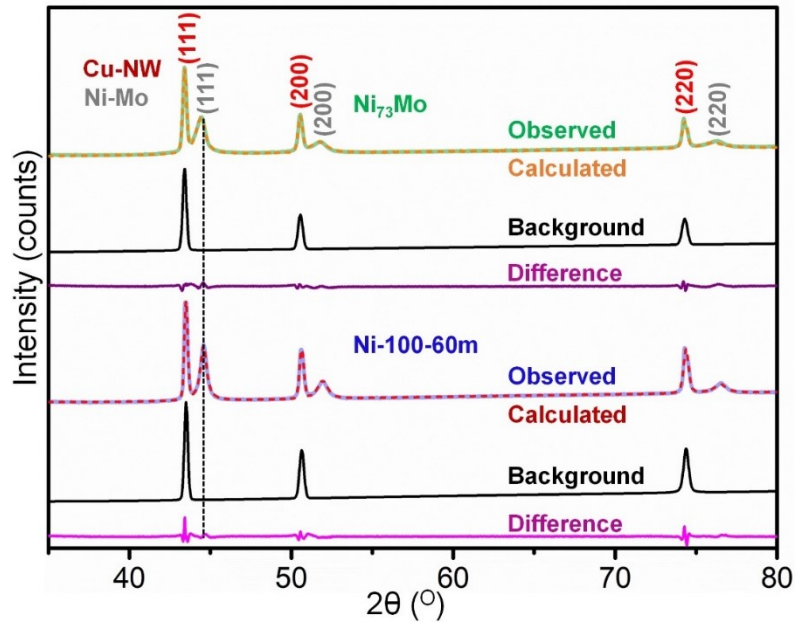
Figure S1. Rietveld refined XRD patterns of Ni$_{73}$Mo and Ni-100-60m.

Table S2. XRD-Rietveld refinement parameters.

Here R$_{wp}$ (weighted profile factor) = $\sqrt{\dfrac{\sum\limits_{i=1}^{N}\left[W_i\left(I^{exp}_i - I^{calc}_i\right)\right]^2}{\sum\limits_{i=1}^{N}\left[W_i I^{exp}_i\right]^2}}$, $w_i = \dfrac{1}{\sqrt{I^{exp}_i}}$, N = number of data points, I^{exp} = observed intensity, I^{calc} = calculated intensity, P = number of parameters. GOF = goodness of fit.

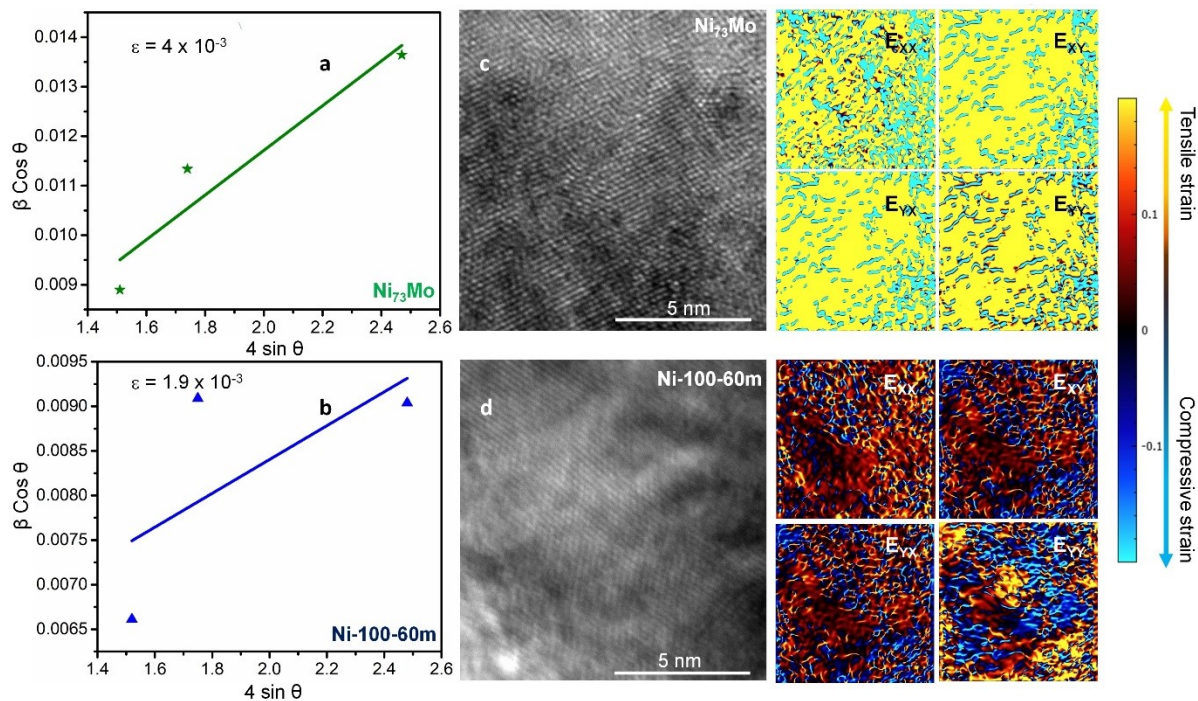| Sample [space group]	Composition	Lattice parameter (Å)	Lattice Volume (Å^3)	Atomic positions (x, y, z)	GOF	R$_{WP}$
Ni-100-60m (*Fm3m*)	Ni 1 Mo 0	$a = b = c$ = 3.5289 $\alpha = \beta = \gamma$ = 90°	43. 95	Ni (0,0,0)	4.46	2.52
Ni$_{73}$Mo (*Fm3m*)	Ni 0.985 Mo 0.015	$a = b = c$ = 3.5551 $\alpha = \beta = \gamma$ = 90°	44.93	Ni (0,0,0) Mo (0,0,0)	4.85	2.56

Figure S2. Williamson-Hall plots of (a) Ni$_{73}$Mo and (b) Ni-100-60m. TEM image (lattice vectors *x* and *y* used as a reference for the strain analysis) and contour plots of the strain components *Exx*, *Exy*, and *Eyy* relative to the reference values on the surface of (c) Ni$_{73}$Mo (d) Ni-100-60m.
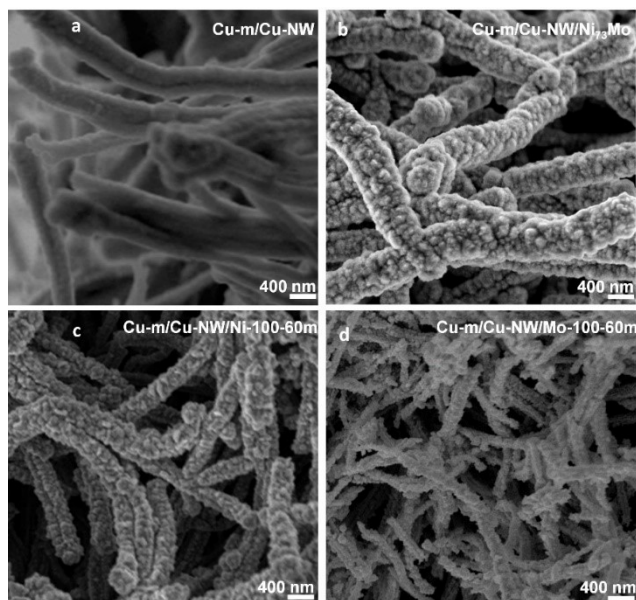

Figure S3. FESEM images of (a) the cross-sectional view of Cu-m/Cu-NW substrate, (b) Cu-m/Cu-NW/Ni$_{73}$Mo, (c) Cu-m/Cu-NW/Ni-100-60m, and (d) Cu-m/Cu-NW/Mo-100-60m.
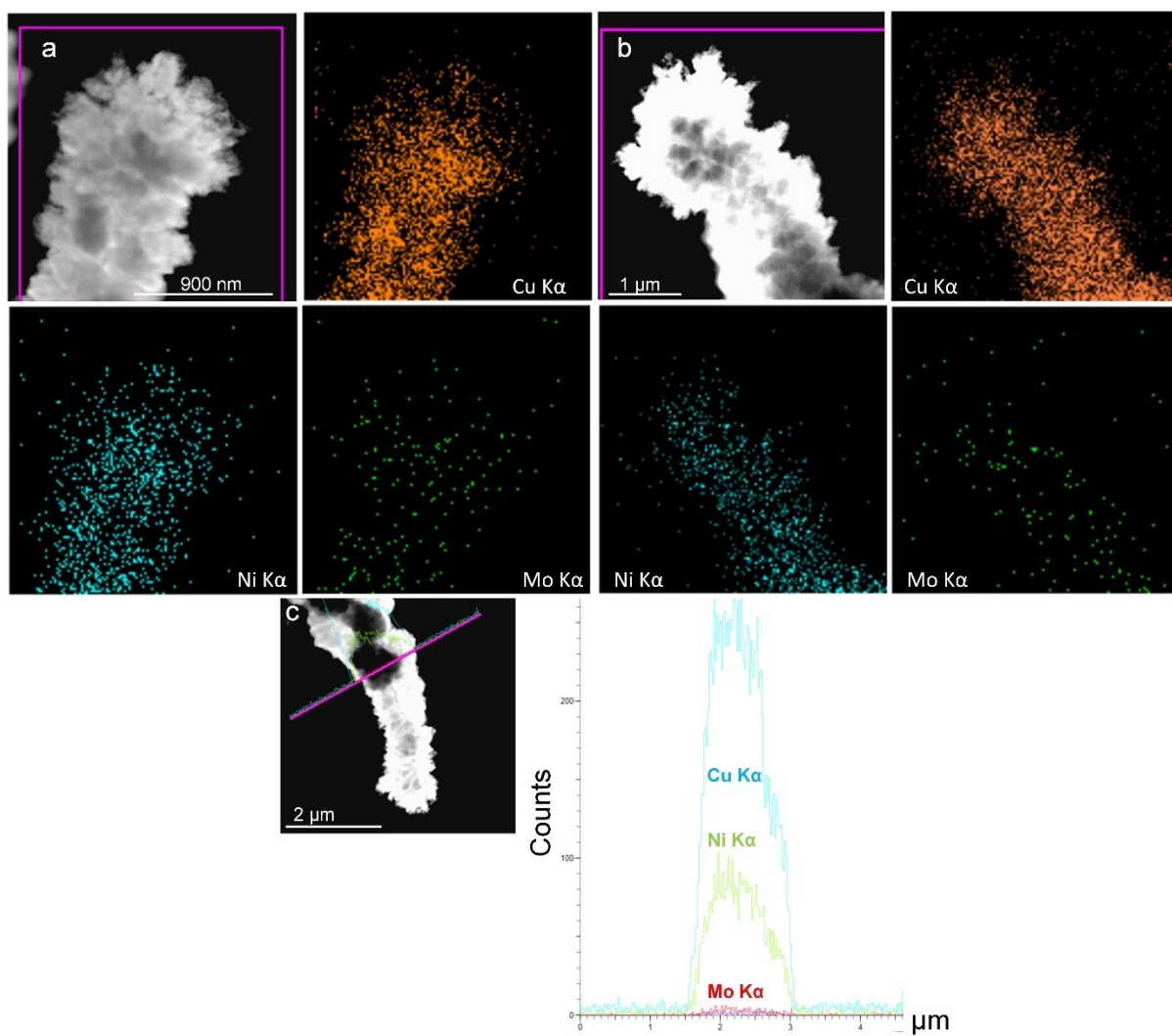
Figure S4. (a, b) HAADF-STEM mapping of Cu-m/Cu-NW/Ni$_{73}$Mo at different positions of the self-supported electrode. (c) Elemental line-scan of Cu-m/Cu-NW/Ni$_{73}$Mo electrode.
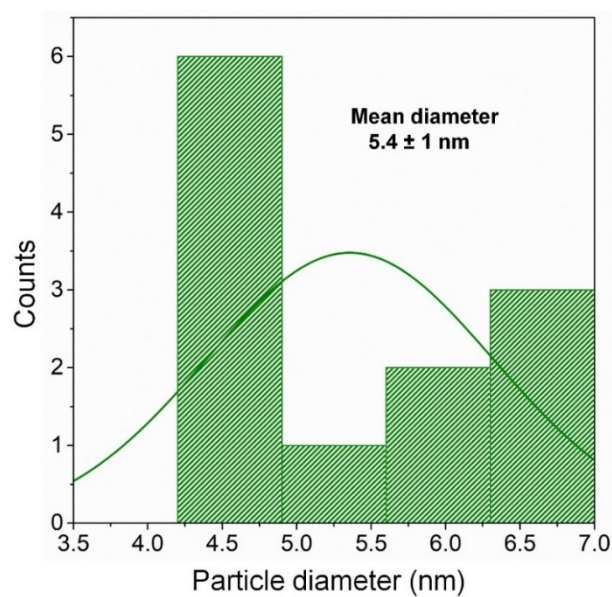

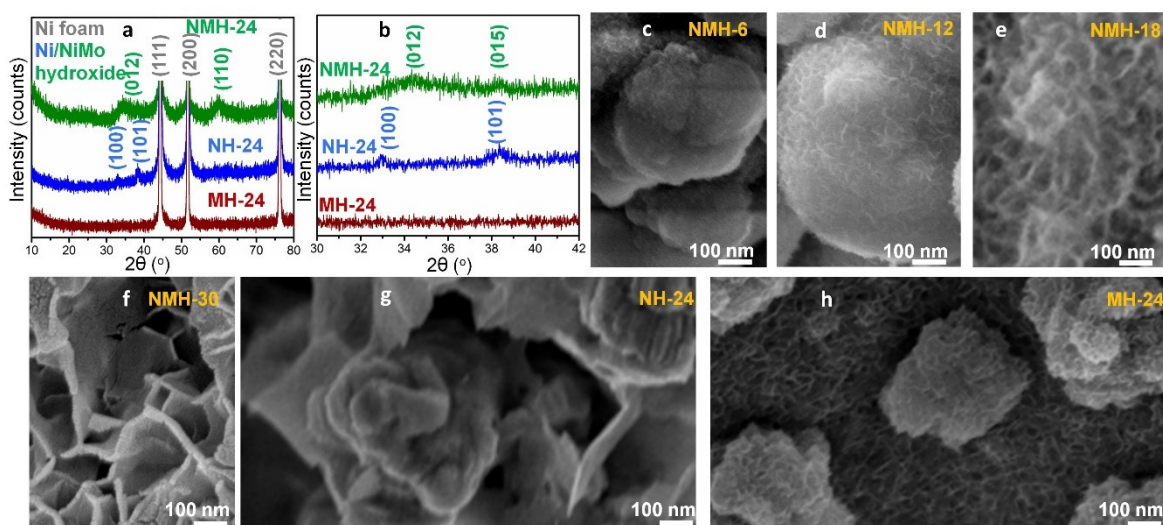**Figure S5.** Size distribution of the Ni$_{73}$Mo nanoparticles.

Figure S6. (a) XRD patterns of NMH-24, NH-24 and MH-24, and (b) their zoomed in XRD patterns in the region 2θ = 30-42°. FESEM images of (c) NMH-6, (d) NMH-12, (e) NMH-18, f) NMH-30, (g) NH-24 and (h) MH-24.
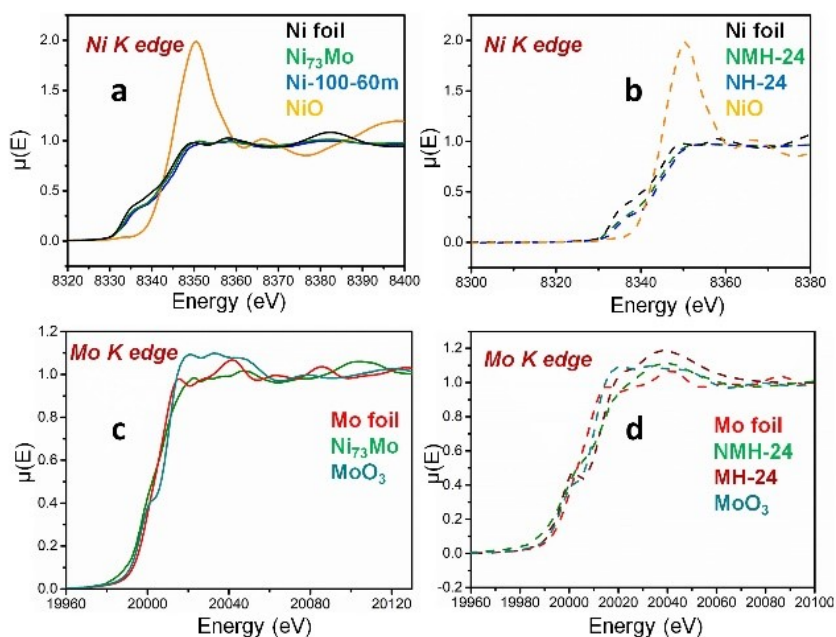

Figure S7. Normalized Ni K edge XANES spectra of (a) Ni foil, $Ni_{73}Mo$, Ni-100-60m, and NiO (b) Ni foil, NMH-24, NH-24, and NiO. Normalized Mo K edge XANES spectra of (c) Mo foil, $Ni_{73}Mo$, and MoO_3 (d) Mo foil, MH-24, MoO_3, and NMH-24.
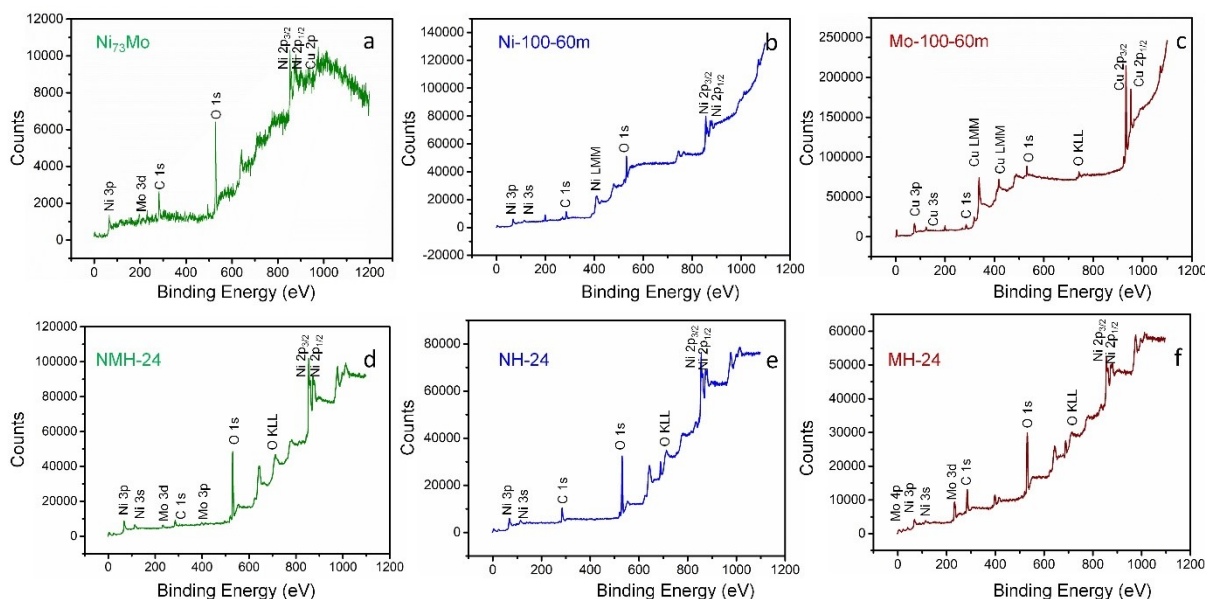
Figure S8. XPS survey spectra of (a) Ni$_{73}$Mo, (b) Ni-100-60m, (c) Mo-100-60m, (d) NMH-24, (e) NH-24, and (f) MH-24.

For the Mo-100-60m spectra, the Mo signal is indiscernible because of the less deposition of Mo on the Cu NW, in corroboration with the XRD pattern, where no prominent reflection from Mo is present (Figure 1c). For Ni$_{73}$Mo and Ni-100-60m, the signal to noise ratio of Cu *2p* level is weak, since the surface of the Cu mesh is covered by the catalysts (loading: 4 mg cm^{-2}).
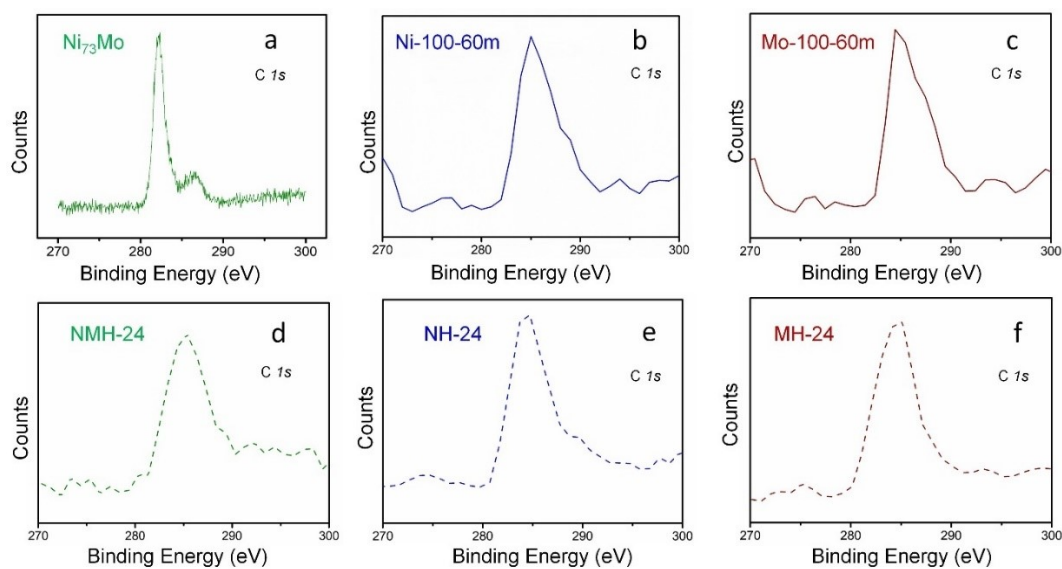

Figure S9. C *1s* spectra from the raw data of (a) Ni$_{73}$Mo, (b) Ni-100-60m, (c) Mo-100-60m, (d) NMH-24, (e) NH-24, and (f) MH-24. The C-C bonds in C *1s* level have binding energy values of 282.3, 285, 284.9, 285.3, 284.3, and 284.8 eV for Ni$_{73}$Mo, Ni-100-60m, Mo-100-60m, NMH-24, NH-24, and MH-24, respectively. The shift in C-C binding energy from the standard value of 284.8 eV was estimated and this difference was used to correct the binding energies of all the elements in a particular sample.
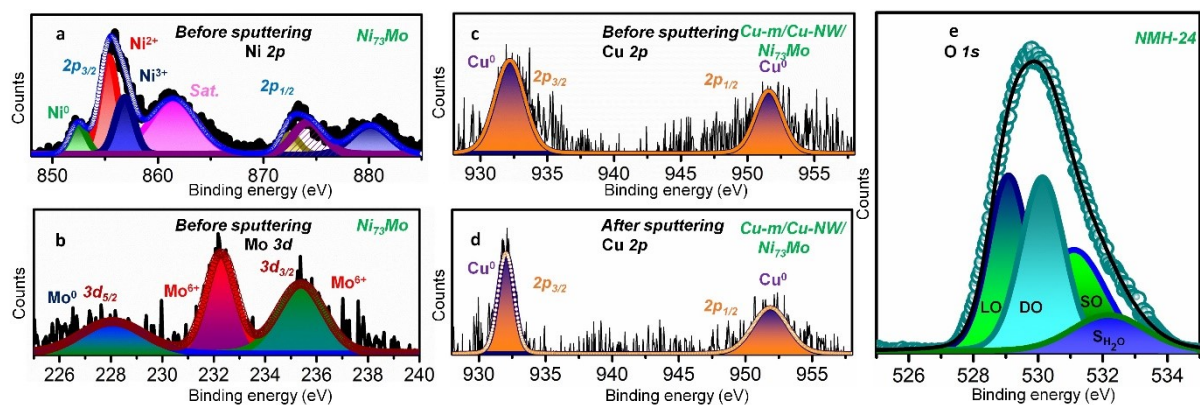
Figure S10. Deconvoluted XPS of (a) Ni *2p* and (b) Mo *3d* levels of Ni$_{73}$Mo before Ar$^+$ sputtering, Cu *2p* level of Cu-m/Cu-NW/Ni$_{73}$Mo (c) before and (d) after Ar$^+$ sputtering, and (e) O *1s* level in NMH-24. LO, DO, SO, and S$_{H2O}$ denote lattice oxygen, defect oxygen, surface adsorbed OH$^-$ and surface adsorbed H$_2$O.

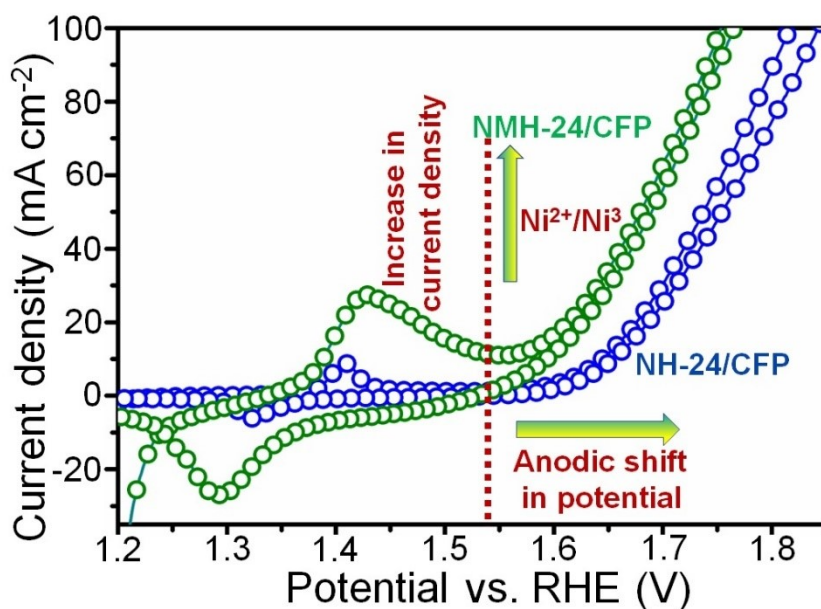**Figure S11.** CV polarization plots of NMH-24 and NH-24 on CFP in 1 M KOH exhibiting the Ni^{2+}/Ni^{3+} redox peak. (Reference electrode Ag/AgCl - 3 M KCl, Counter electrode – Pt wire, Scan rate – 10 mV/s)
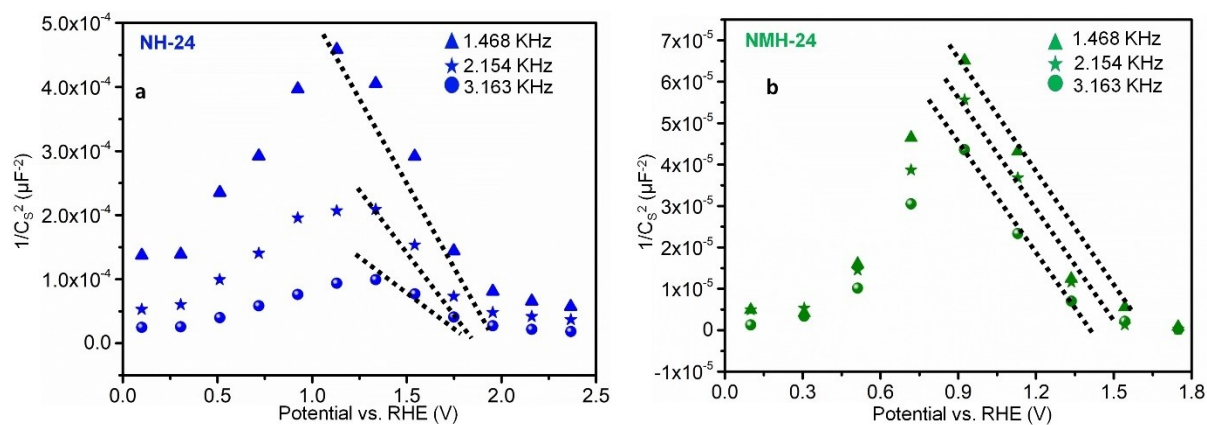
Figure S12. Fitted Mott-Schottky plots of (a) NH-24 and (b) NMH-24.

Table S3. Bader charge analyses of Mo-doped Ni (111) system, for $Ni_{79}Mo$.

Nearby Ni-atoms	Ni (surf)	Ni (surf)	Ni (surf)	Ni (surf)	Ni (surf)	Ni (surf)	Ni[2nd] layer	Ni[2nd] layer	Ni[2nd] layer	Mo
charge	-0.12	-0.12	-0.13	-0.13	-0.12	-0.12	-0.09	-0.1	-0.08	**1.10**

Table S4. Surface Mo-Ni distances for Ni_4Mo. The respective metal sites are shown in Figure S9.

Bond	Mo-Ni1	Mo-Ni2	Mo-Ni3	Mo-Mo4	Mo-Ni5	Mo-Ni6	Mo-Ni7	Mo-Mo8	Mo-Mo9
Bond distances (Å)	2.5	2.54	2.5	2.58	2.57	2.64	2.85	2.86	2.64

Table S5. Bader charge values of the circled Mo-center in Figure S9, and the surrounding Mo and Ni atoms, for Ni_4Mo. Here 'Mo' represents the highlighted Mo.

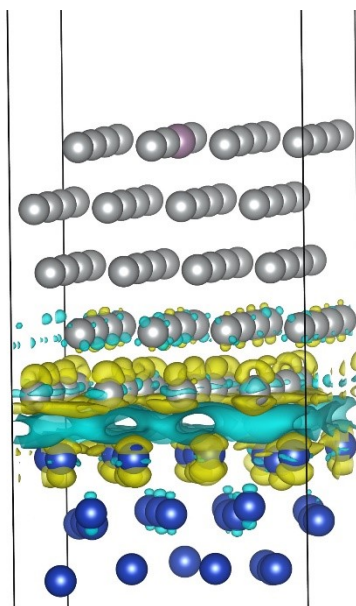| Nearby Ni-atoms	Ni 1	Ni 2	Ni 3	Ni 5	Ni 6	Ni 7	Mo 4	Mo 8	Mo 9	Mo
Charge	-0.3	-0.32	-0.4	-0.43	-0.36	-0.36	0.79	0.81	0.75	0.68

S-9

Figure S13. Charge transfer between Cu substrate and $Ni_{73}Mo$ alloy. Isosurface value is taken as 0.002 e $Å^{-3}$. The yellow and cyan color represent the charge depletion and accumulation, respectively.
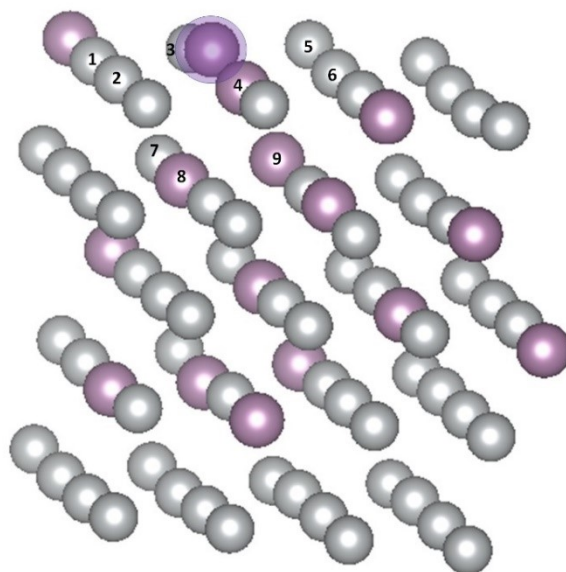

Figure S14. Computational model structure of Ni_4Mo. This model has been used to determine the surface Mo-Ni distances (Table S3) and Bader charge values (Table S4).
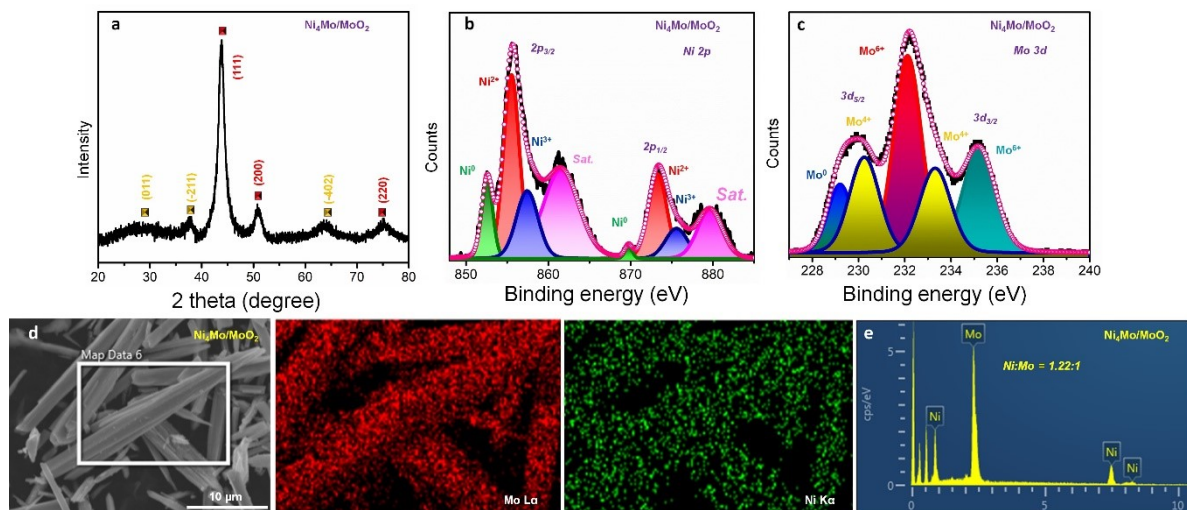
Figure S15. Characterization of Ni$_4$Mo/MoO$_2$ catalyst. (a) XRD pattern, deconvoluted XPS of (b) Ni *2p* and (c) Mo *3d* levels, (d) elemental mapping, and (e) EDS of Ni$_4$Mo/MoO$_2$.

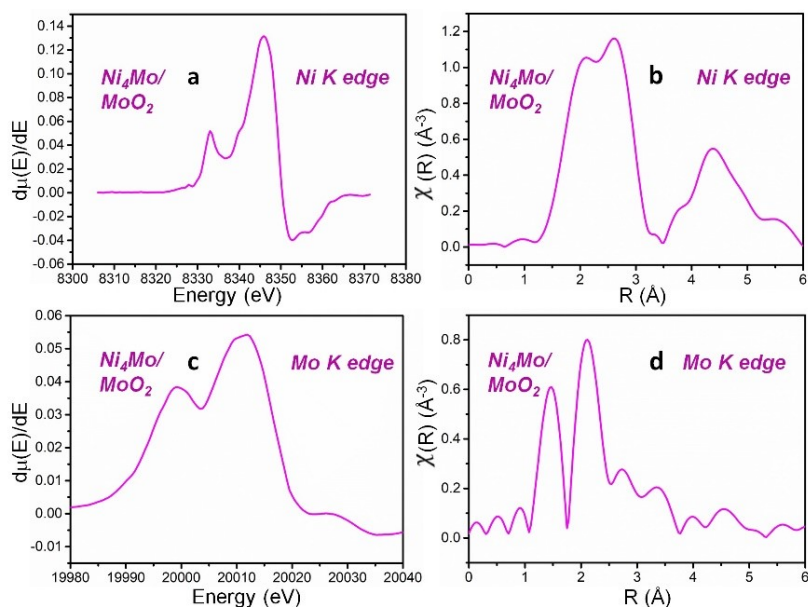**Figure S16.** (a) First derivative Ni *K* edge XANES and (b) Fourier Transform of k^2-weighted $\chi(R)$ spectra (phase corrected) at Ni *K* edge spectra of Ni$_4$Mo/MoO$_2$. (c) First derivative Mo *K* edge XANES and (d) Fourier Transform of k^2-weighted $\chi(R)$ spectra (phase corrected) at Mo *K* edge spectra of Ni$_4$Mo/MoO$_2$.
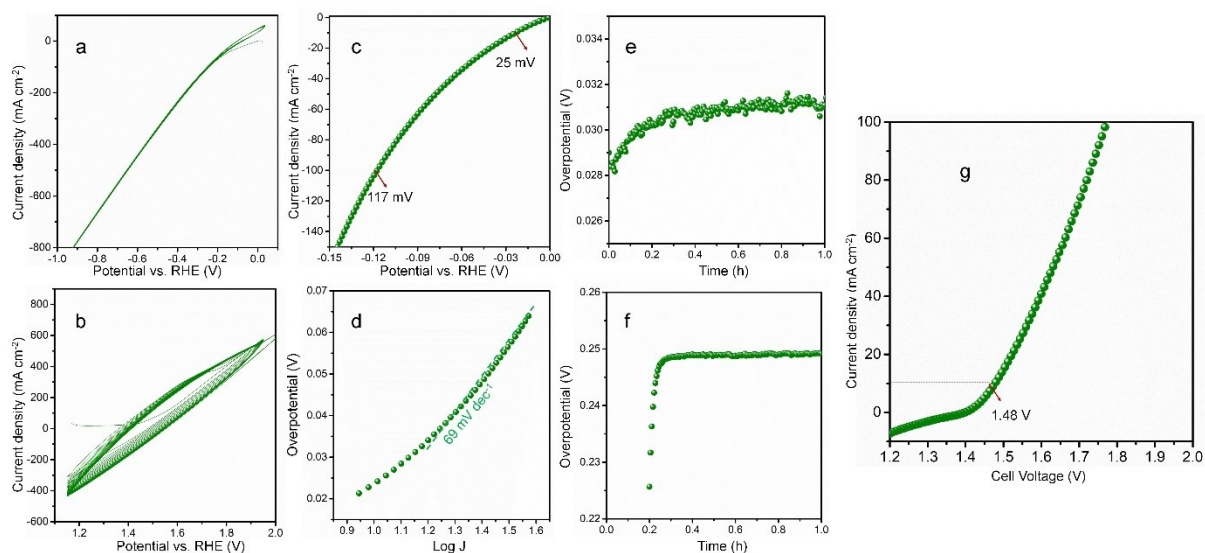
S-11

Figure S17. CV saturation plots of (a) $Ni_{73}Mo$, and (b) NMH-24 electrodes taken prior to recording the LSV polarization curves. (c) LSV polarization curve of $Ni_{73}Mo$ in backward scan at 1 mV s^{-1} scan rate, and (d) the corresponding Tafel plot. Chronopotentiometry of (e) $Ni_{73}Mo$ at -10 mA cm^{-2}, and (f) NMH-24 at -10 mA cm^{-2}. (g) LSV polarization curve of NMH-24 (+) || $Ni_{73}Mo$ (-) in backward scan at 5 mV s^{-1} scan rate. All these measurements were conducted in 1 M KOH electrolyte.
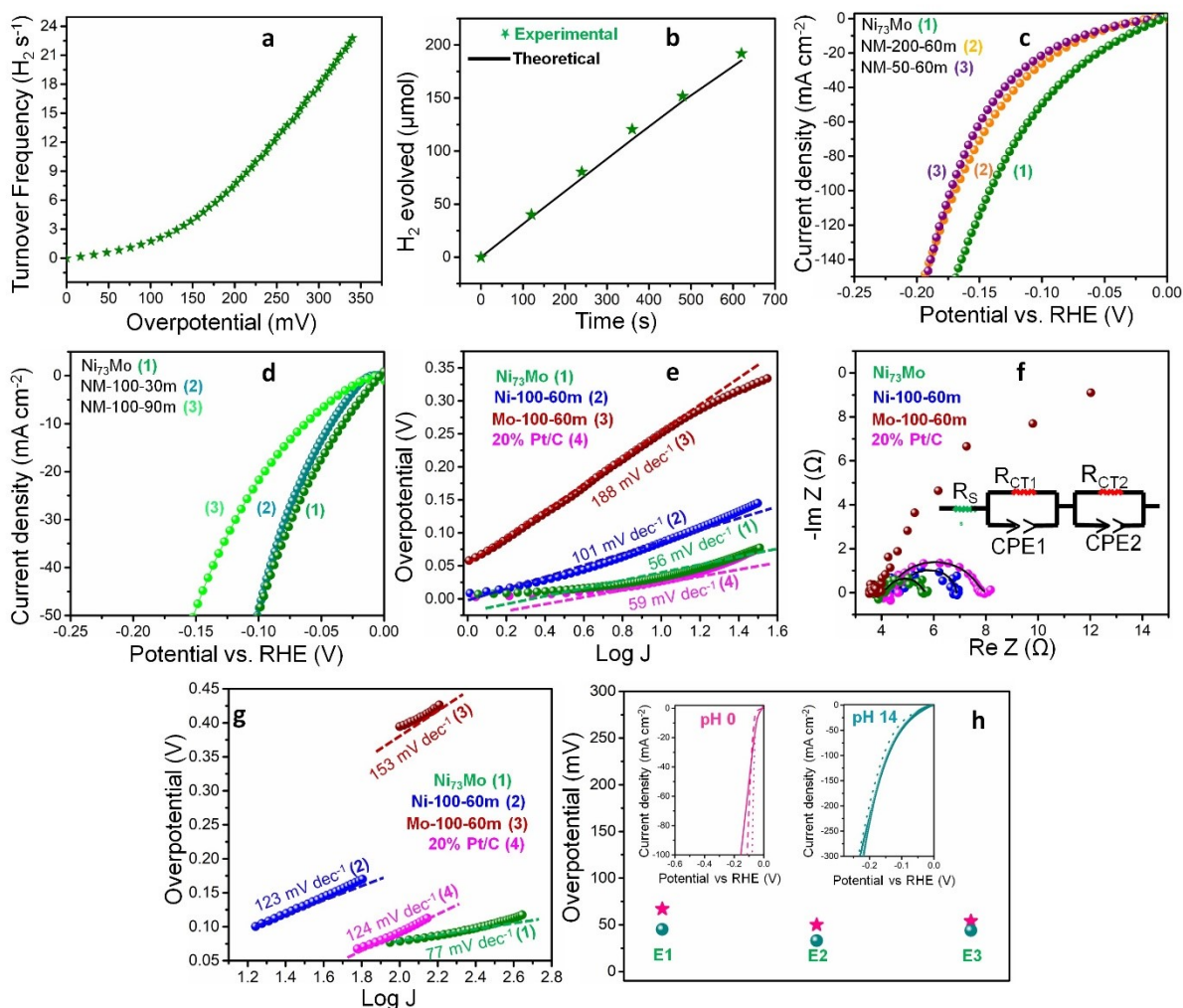
Figure S18. (a) TOF of Ni$_{73}$Mo in 1 M KOH as a function of HER overpotentials versus RHE. (b) Faradaic efficiency of Ni$_{73}$Mo at an overpotential of 484 mV (*iR*-uncorrected). (c) HER polarization curves (*iR*-corrected) in 1 M KOH for Ni$_{73}$Mo, and the samples prepared by electrodeposition at -50 mA cm^{-2} (NM-50-60m) and -200 mA cm^{-2} (NM-200-60m). (d) HER polarization curves (*iR*-corrected) in 1 M KOH for Ni$_{73}$Mo, and the samples prepared by electrodeposition at -100 mA cm^{-2} for 30 min (NM-100-30m) and 90 min (NM-100-90m). (e) Tafel slopes of Ni$_{73}$Mo, Ni-100-60m, Mo-100-60m and 20% Pt/C in 1 M KOH. (f) Nyquist plots of Ni$_{73}$Mo, 20% Pt/C Ni-100-60m and Mo-100-60m in 1 M KOH at an overpotential of 234 mV (iR-uncorrected). The inset represents the equivalent circuit. (g) Tafel slopes of Ni$_{73}$Mo, 20% Pt/C, Ni-100-60m and Mo-100-60m in 0.5 M H$_2$SO$_4$. (h) Reproducibility test of Ni$_{73}$Mo in 1 M KOH and 0.5 M H$_2$SO$_4$. Insets show the corresponding LSV polarization curves of the electrodes synthesized in different batches.
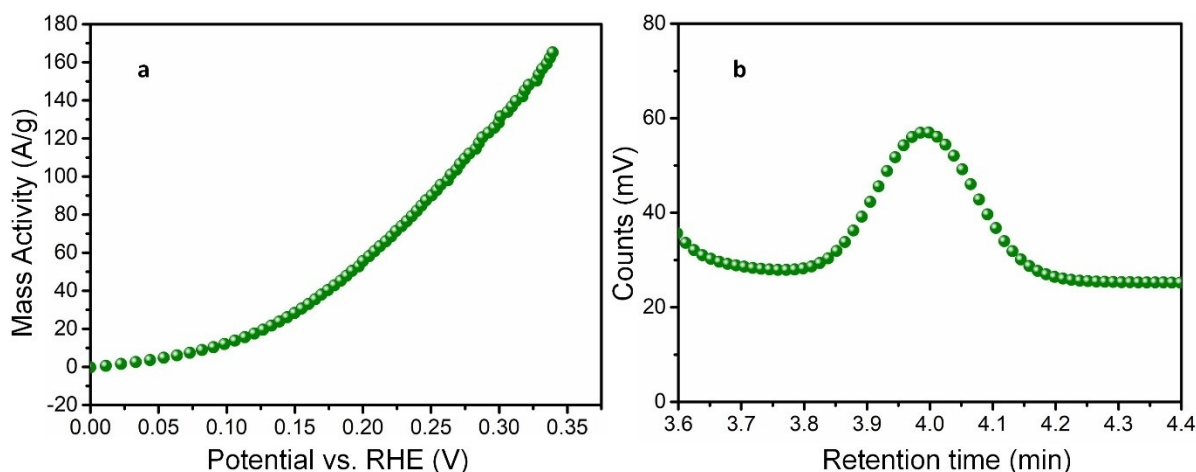
Figure S19. (a) Mass activity of $Ni_{73}Mo$ in 1 M KOH considering 4 mg cm^{-2} catalyst loading. (b) GC analysis of $Ni_{73}Mo$ in 1 M KOH.
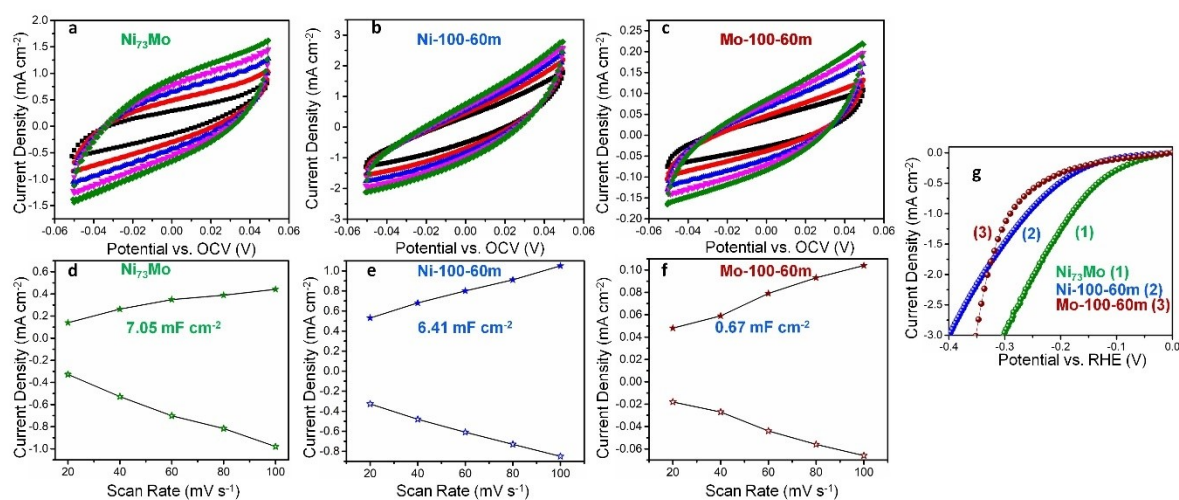

Figure S20. ECSA determination in 1 M KOH. CV plots of (a) $Ni_{73}Mo$, (b) Ni-100-60m, and (c) Mo-100-60m, at different scan rates. Plots of current density (recorded at a fixed potential) as a function of scan rate for (d) $Ni_{73}Mo$, (e) Ni-100-60m, and (f) Mo-100-60m. (g) ECSA normalized LSV polarization plots for Mo-100-60m, Ni-100-60m and $Ni_{73}Mo$.

The linear fits of current versus scan rate plots are extrapolated to 0 mV s^{-1}. For an ideal capacitor, the intercept value of these linear plots should be 0 mA cm^{-2}, where the CV plots are completely reversible. In this work, the electrodes do not behave like an ideal capacitor. Therefore, positive intercept values are obtained as 0.1, 0.41, and 0.03 mA cm^{-2} and negative intercept values as -0.19, -0.21, and -0.005 mA cm^{-2} for $Ni_{73}Mo$, Ni-100-60m, and Mo-100-60m, respectively.

Table S6. Parameters obtained from the EIS fitting for HER and OER.

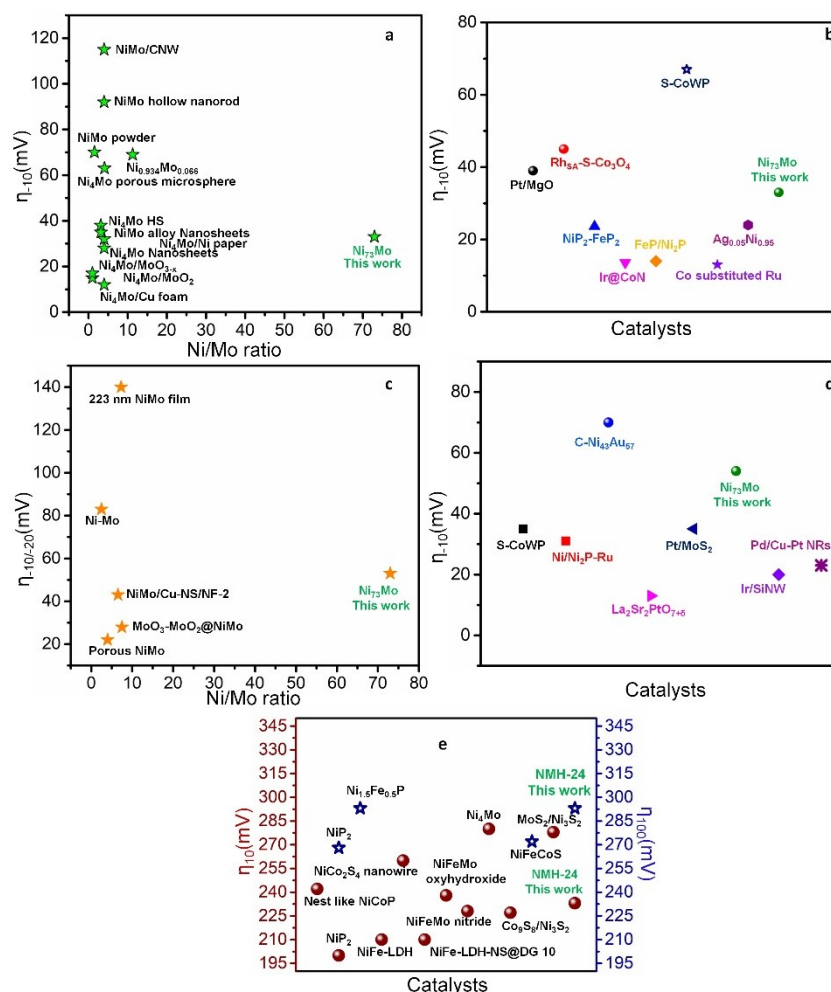| Catalyst	R_s (Ω)	R_{CT1} (Ω)	R_{CT2} (Ω)
Ni$_{73}$Mo	3.2	1.3	1.24
Ni-100-60m	4.6	0.34	1.9
20% Pt-C	4.07	2.87	1.09
NMH-24	3.67	2.42	6.9
NH-24	3.8	0.745	10.4
MH-24	3.65	0.36	18.8
RuO$_2$	3.47	2.78	6.25

Figure S21. (a) Scattered plot for literature reported HER activities at -10 mA cm^{-2} in 1 M KOH with different Ni/Mo ratios: *Ref. (S1) Ni$_4$Mo/Ni paper, (S2) Ni$_4$Mo/MoO$_2$, (S3) Ni$_4$Mo/MoO$_{3-x}$, (S4) Ni$_4$Mo/CNW, (S5) Ni$_4$Mo porous microsphere, (S6) Ni$_4$Mo nanosheet, (S7) Ni$_4$Mo/Cu foam, (S8) Ni$_{0.934}$Mo$_{0.066}$, (S9) Ni$_4$Mo HS, (S10) NiMo alloy nanosheet, (S11) Ni$_4$Mo hollow nanorod, (S12) NiMo nanopowder.* (b) Scattered plot of overpotentials at -10 mA cm^{-2} for literature reported non-Ni-Mo based HER catalysts in alkaline medium. *Ref. (S13) Pt/MgO, (S14) Rh$_{SA}$-S-Co$_3$O$_4$, (S15) NiP$_2$-FeP$_2$, (S16) Ir@CoN, (S17) FeP/Ni$_2$P, (S18) S-CoWP, (S19) Co substituted Ru, (S20) Ag$_{0.05}$Ni$_{0.95}$.* (c) Scattered plot for literature reported HER activities in 0.5 M H$_2$SO$_4$ with different Ni/Mo ratios: *Ref. (S21) Porous NiMo, (S22) MoO$_3$-MoO$_2$@NiMo, (S23) NiMo/Cu nanosheet/Ni foam, at -10 mA cm^{-2}, and (S24) Ni-Mo, (S25) 170 nm NiMo, at -20 mA cm^{-2}.* (d) Scattered plot of overpotentials at -10 mA cm^{-2} for literature reported non-Ni-Mo based HER catalysts in acidic medium. *(S18) S-CoWP, (S26) Ni/Ni$_2$P-Ru, (S27) Pt-WO$_3$, (S28) La$_2$Sr$_2$PtO$_{7+\delta}$ (S29) Pt/MoS$_2$, (S30) Ir/SiNW, (S31) Pd/Cu-Pt NRs.* (e) Scattered plot of overpotentials at -10 mA cm^{-2} for literature reported OER catalysts. *Ref. (S32) NiFeMo nitride, (S33) NiFeMo oxyhydroxide, (S34) NiFe-LDH-NS@DG10, (S35) Ni$_2$P, (S36) Co$_9$S$_8$/Ni$_3$S$_2$, (S37) Ni$_4$Mo, (S38) NiCo$_2$S$_4$ nanowire, (S39) nest-like NiCoP, (S40) NiFeCoS, (S41) Ni$_{1.5}$Fe$_{0.5}$P, (S42) NiFe-LDH.*
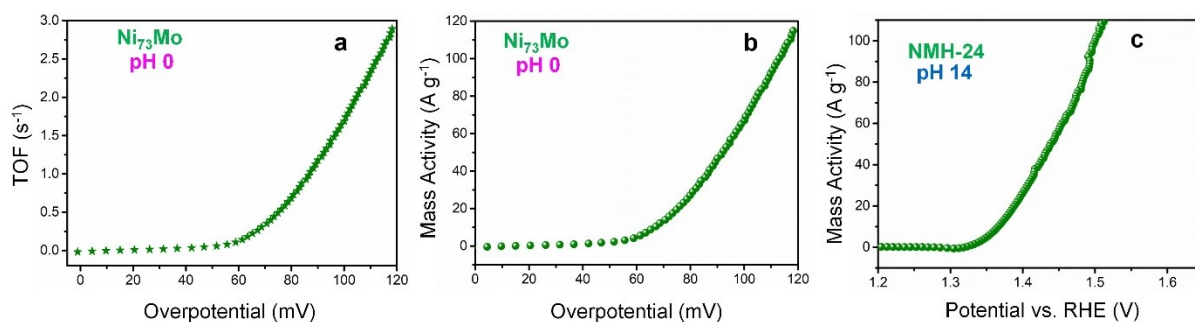
Figure S22. (a) TOF, and (b) mass activity of $Ni_{73}Mo$ in 0.5 M H_2SO_4 as a function of HER overpotentials versus RHE. (c) Mass activity of NMH-24 in 1 M KOH + 0.33 M urea as a function of potentials versus RHE.

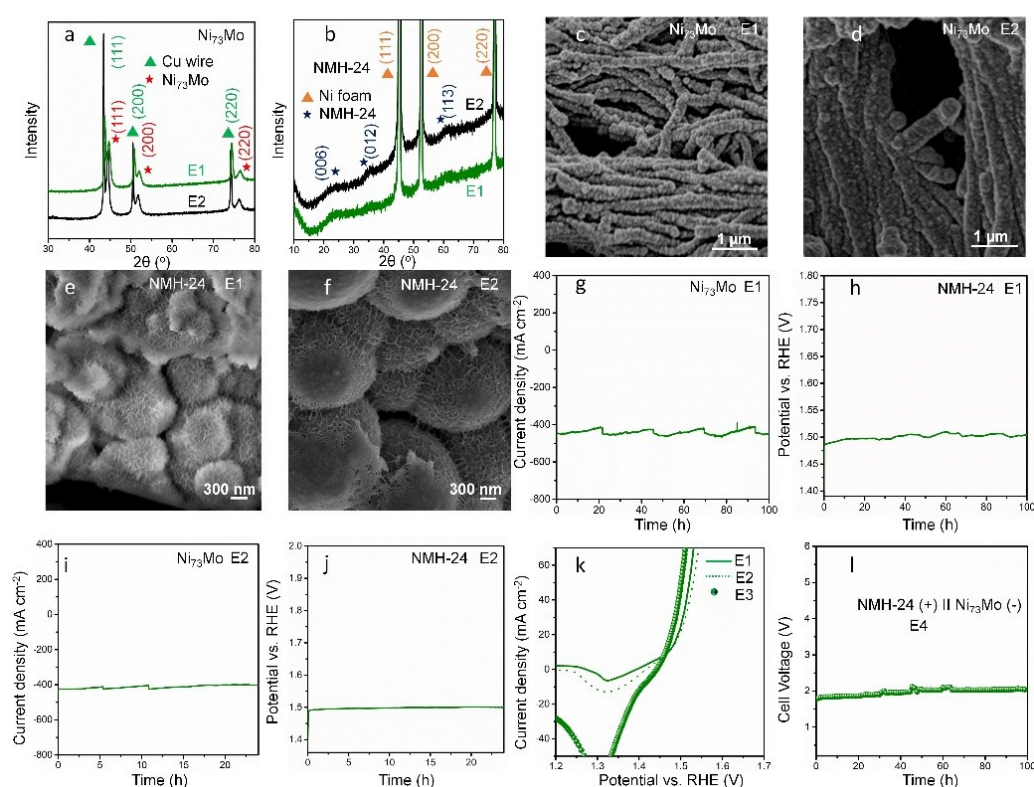**Figure S23.** XRD patterns of (a) $Ni_{73}Mo$, and (b) NMH-24 electrodes synthesized in two different batches. FESEM images of (c, d) $Ni_{73}Mo$, and (e, f) NMH-24 electrodes synthesized in two different batches. (g) Chronoamperometry tests of $Ni_{73}Mo$ for 100 h using Pt counter electrode at a potential of -0.534 V versus RHE. (h) Chronopotentiometric stability test of NMH-24 for 100 h at 20 mA cm^{-2} using Pt counter electrode. (i) Chronoamperometry tests of $Ni_{73}Mo$ for 24 h using graphite counter electrode at a potential of -0.534 V versus RHE. (j) Chronopotentiometric stability test of NMH-24 for 24h at 20 mA cm^{-2} using graphite counter electrode. (k) OER polarization curves (*iR*-corrected) for NMH-24 at a scan rate of 1 mV s^{-1} in backward scan synthesized in different batches. (l) Reproducibility of overall stability for 100 h using Ni foam/NMH-24 (+) || Cu-mesh/Cu-NW/$Ni_{73}Mo$ (-) at a current density of 100 mA cm^{-2}. The measurements were conducted in 1 M KOH electrolyte.

Table S7. The changes in free energy of adsorption of H_2O^*, H^* and OH^* on Ni (111), Pt (111) and $Ni_{79}Mo$ systems.

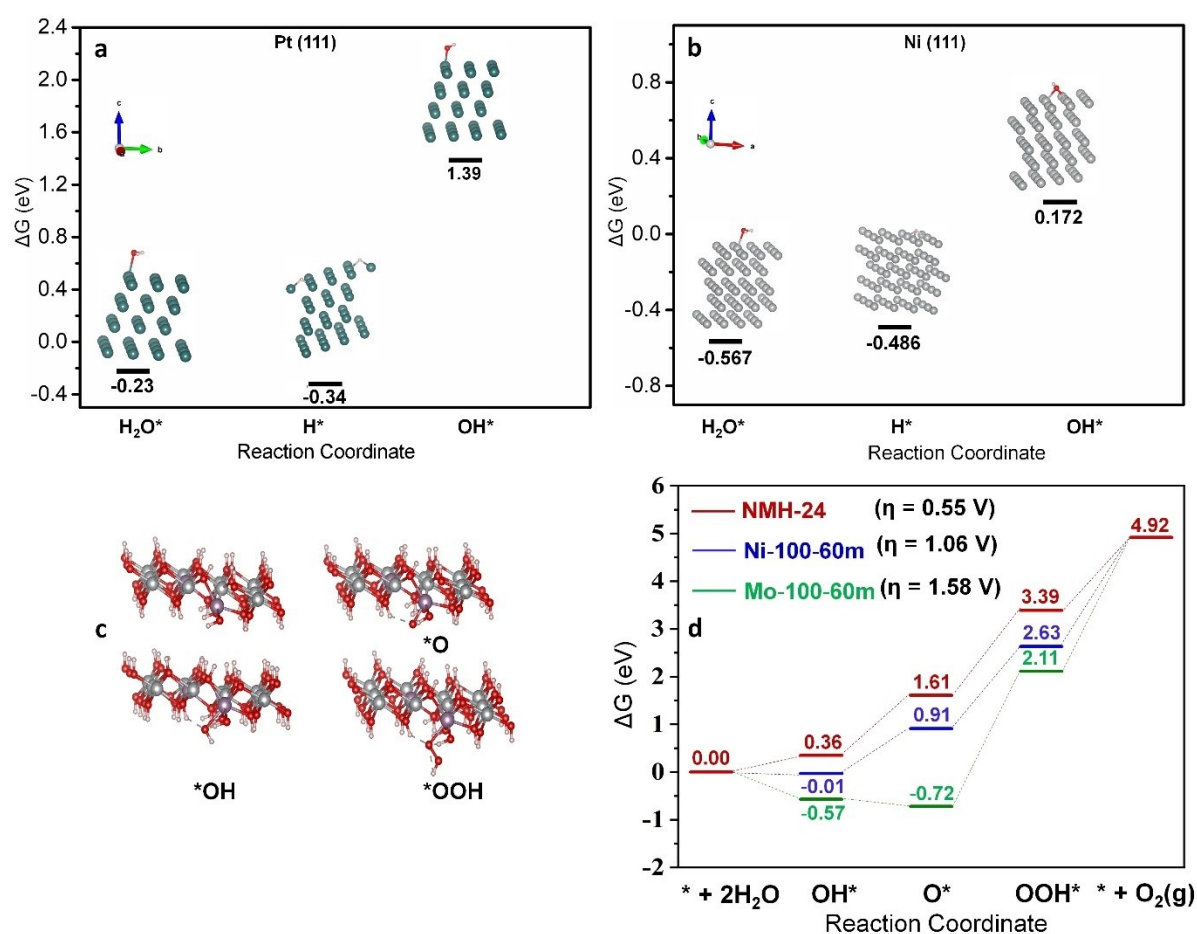| ΔG	H₂O*	H* (3-centered)	OH*
Ni (111)	-0.57	-0.49	0.17
Pt (111)	-0.23	-0.34	1.39
Ni₇₉Mo	-1.03 (Mo-top) -0.57 (Nearest Ni-top) -0.64 (Next-nearest Ni-top)	-0.55 (Mo-top) -0.52 (Nearest Ni-top) -0.35 (Next-nearest Ni-top)	-0.45 (Mo-top) -0.41 (Nearest Ni-top) 0.3 (Next-nearest Ni-top)

Figure S24. The changes in free energy of adsorption (ΔG) of reactant (H₂O*) and intermediates (H* and OH*) on (a) Pt (111) system, and (b) Ni (111) system. The H* intermediate is considered to be adsorbed on 3-centered Ni-site. (c) Optimized geometries of the intermediates during OER on NMH-24. (d) Free energy diagram for OER on NMH-24, Ni-100-60m and Mo-100-60m catalysts.
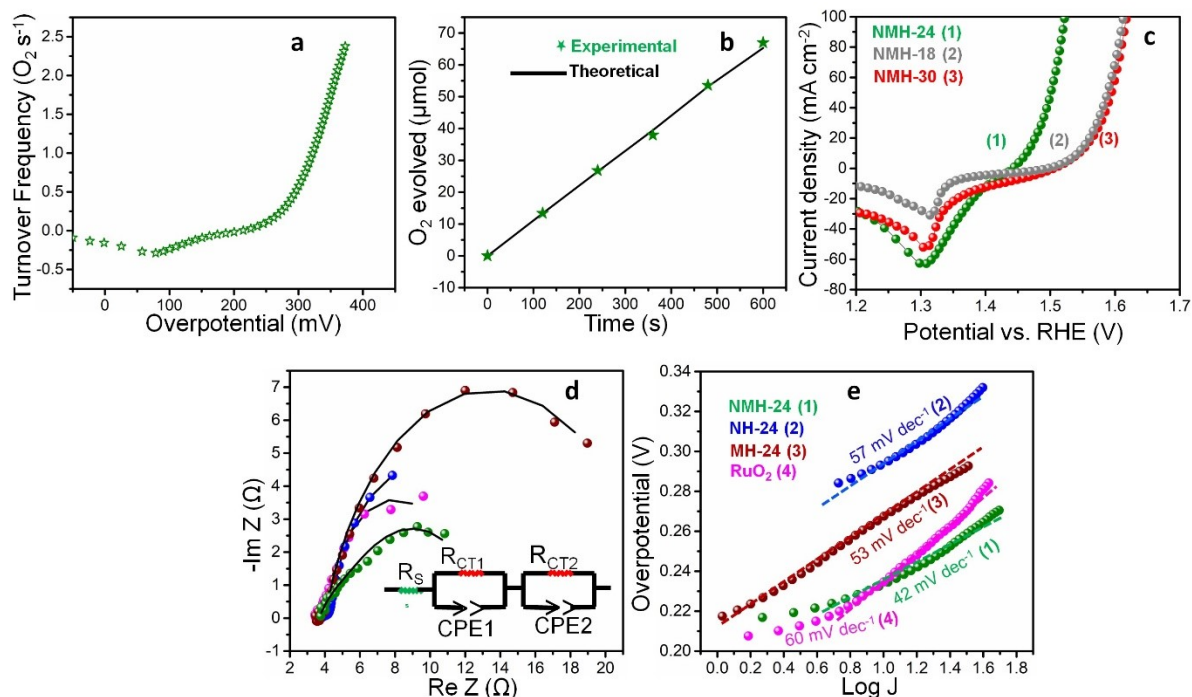
Figure S25. (a) TOF of NMH-24 in 1 M KOH as a function of overpotentials versus RHE. (b) Faradaic efficiency of NMH-24 at an overpotential of 536 mV (*iR*-uncorrected). (c) OER polarization curves (*iR*-corrected) of NMH-18, NMH-24 and NMH-30 in 1 M KOH, prepared with different electrodeposition times. (d) Nyquist plots of NMH-24, NH-24, MH-24 and RuO_2 in 1 M KOH at an overpotential of 336 mV (*iR*-uncorrected). The inset represents the equivalent circuit. (e) Tafel slopes of NMH-24, NH-24, MH-24 and RuO_2 in 1 M KOH.
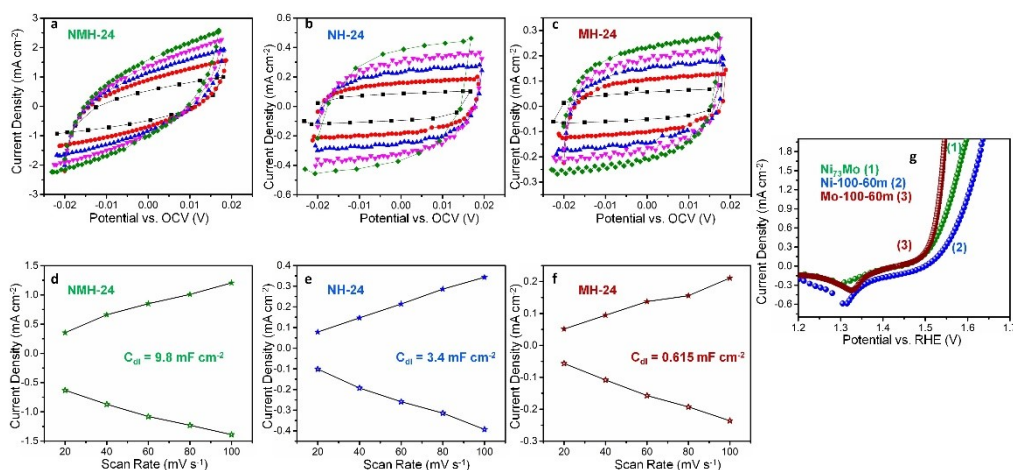

Figure S26. ECSA determination in 1 M KOH. CV plots of (a) NMH-24, (b) NH-24 and (c) MH-24, at different scan rates. Plots of current density (recorded at a fixed potential) as a function of scan rate for (d) NMH-24, (e) NH-24 and (f) MH-24. (g) ECSA normalized LSV polarization plots for NMH-24, NH-24 and MH-24.

Since the electrodes behave as non-ideal capacitors, the intercepts slightly deviate from the ideal 0 mA cm^{-2}. The positive intercept values of 0.2, 0.01, and 0.02 mA cm^{-2} and negative intercept values of -0.5, -0.04, and -0.002 mA cm^{-2} are obtained for NMH-24, NH-24, and MH-24, respectively.
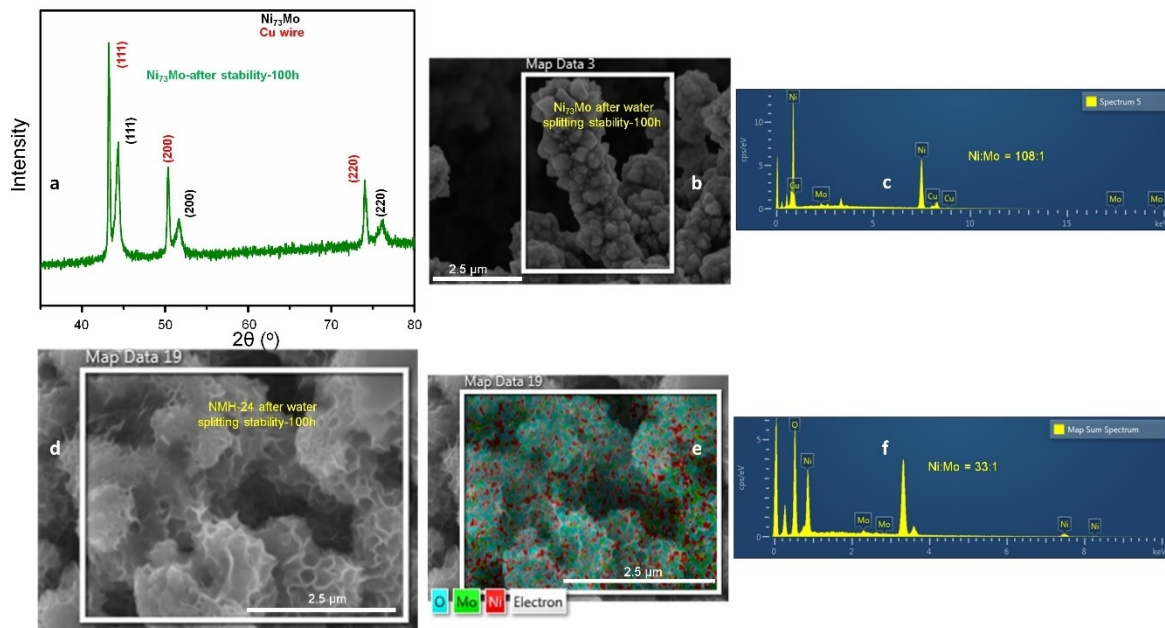
Figure S27. (a) XRD pattern, (b) FESEM, and (c) EDS spectrum of Ni$_{73}$Mo in 1 M KOH after 100 h stability test. (d) FESEM, (e) EDS mapping and (f) EDS spectra of NMH-24 in 1 M KOH after 100 h stability test.
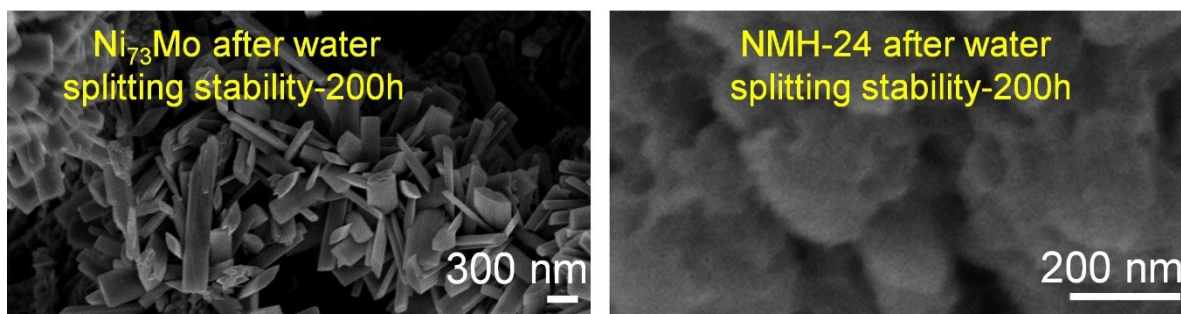

Figure S28. FESEM images of (a) Ni$_{73}$Mo and (b) NMH-24 in 1 M KOH after 200 h full cell stability test.
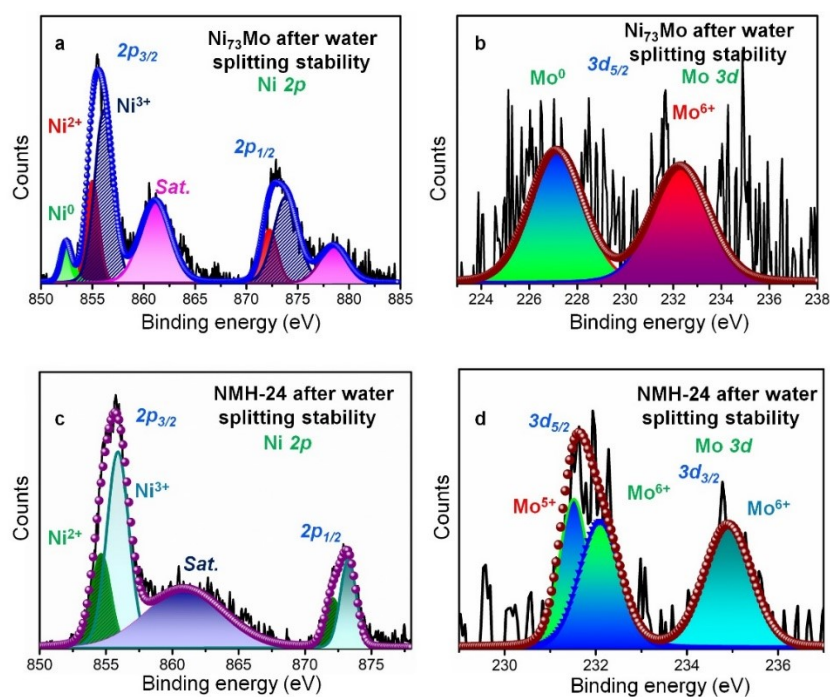
Figure S29. Deconvoluted XPS of (a) Ni *2p*, (b) Mo *3d* levels for Ni$_{73}$Mo, and (c) Ni *2p*, (d) Mo *3d* levels for NMH-24, after the overall water splitting stability test.
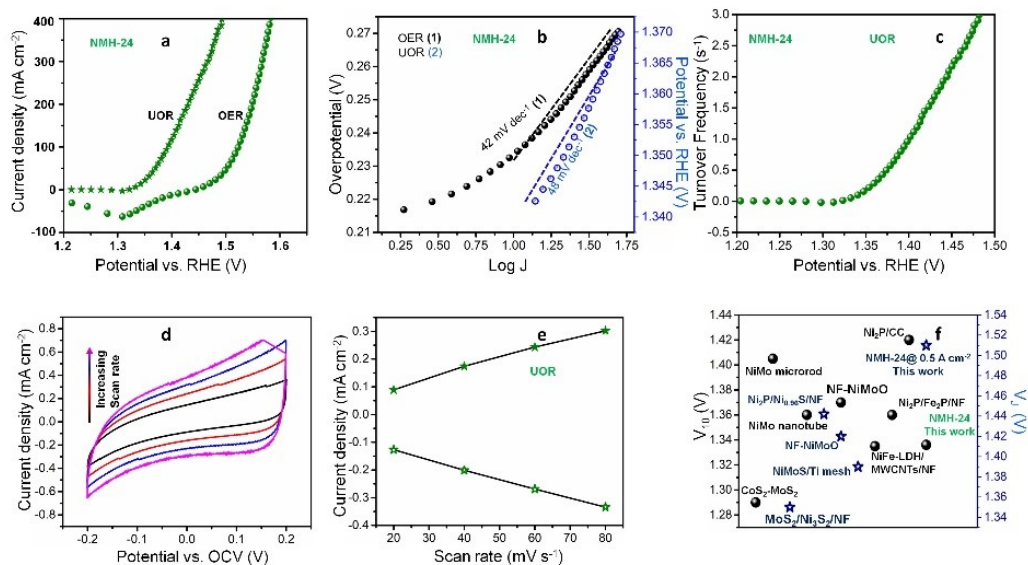

Figure S30. UOR performance of NMH-24 in 1 M KOH + 0.33 M urea. (a) UOR and OER polarization curves (*iR*-corrected) of NMH-24 in 1 M KOH + 0.33 M urea, and 1 M KOH, respectively. (b) Tafel slopes of NMH-24 for UOR and OER. (c) TOF of NMH-24 as a function of overpotentials in 1 M KOH + 0.33 M urea. (d) CV plots for ECSA determination of NMH-24, at different scan rates, and (e) plots of current density (recorded at a fixed potential) as a function of scan rate for NMH-24 in 1 M KOH + 0.33 M urea. (f) Scattered plot for literature reported UOR activities of different catalysts. *Ref. (S43) NF-NiMoO; J = 100 mA cm^{-2}, (S44) NiMo nanotube, (S45) CoS$_2$-MoS$_2$, (S46) Ni$_2$P-Fe$_2$P, (S47) MoS$_2$-Ni$_3$S$_2$; J = 200 mA cm^{-2}, (S48) Ni$_2$P-Ni$_{0.96}$S; J = 100 mA cm^{-2}, (S49) NiFe-LDH/MWCNT/NF, (S50) NiMo microrod, (S51) NiMoS/Ti mesh; J = 60 mA cm^{-2}, (S52) Ni$_2$P.*
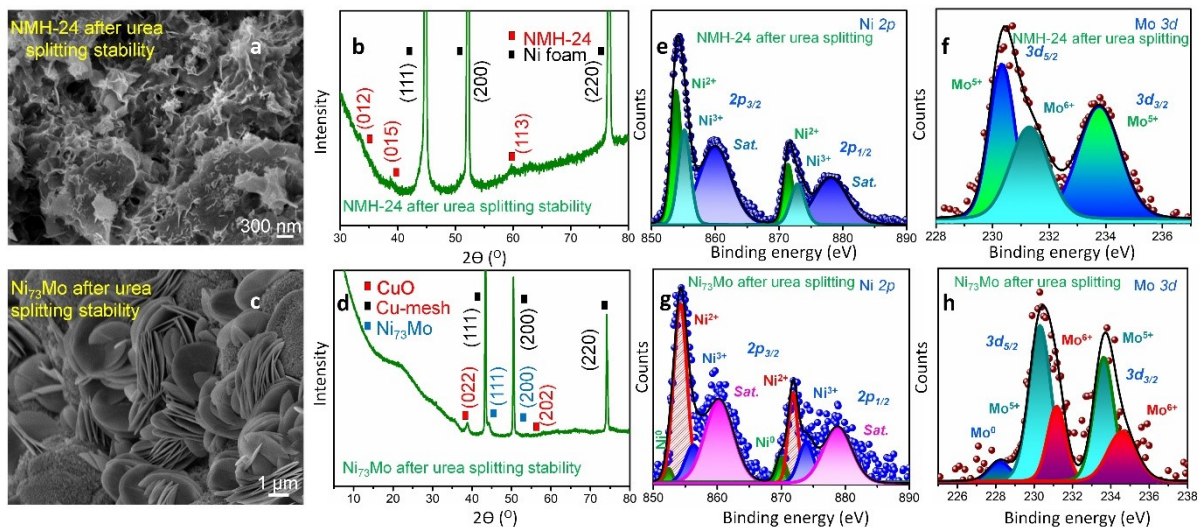
Figure S31. (a) FESEM, and (b) XRD pattern of NMH-24, and (c) FESEM, and (d) XRD pattern of $Ni_{73}Mo$ after the stability test in 1 M KOH + 0.33 M urea electrolyte. XPS analysis of (e) Ni *2p*, and (f) Mo *3d* levels in NMH-24, and (g) Ni *2p*, and (h) Mo *3d* levels in $Ni_{73}Mo$ after urea splitting in 1 M KOH + 0.33 M urea electrolyte.
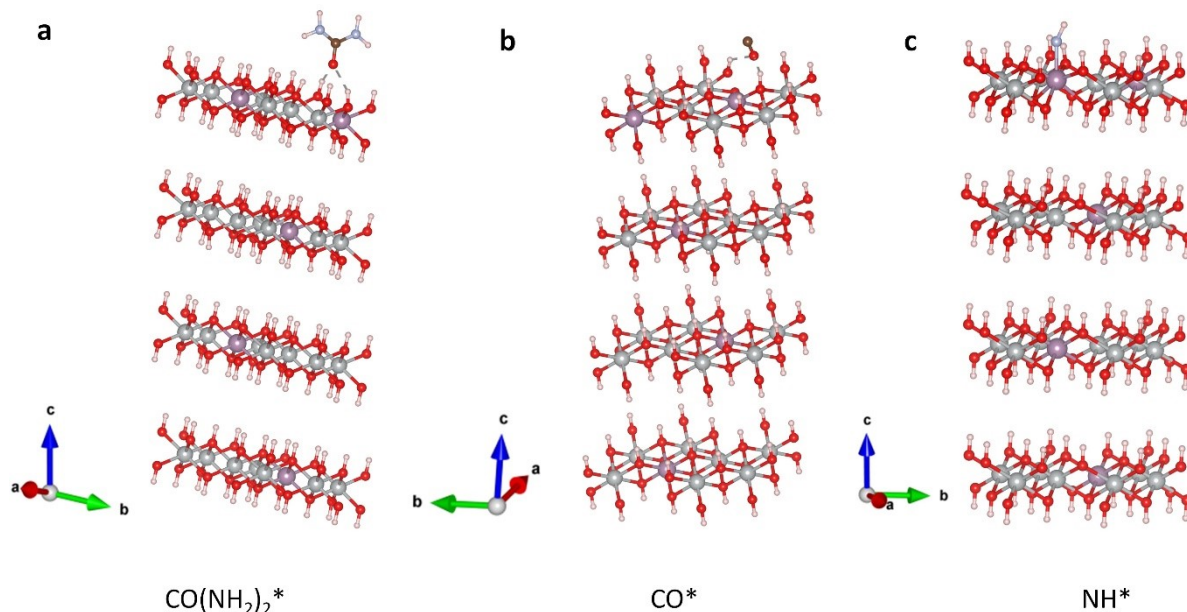
$CO(NH_2)_2*$	$CO*$	$NH*$

Figure S32. The structures of adsorption of the reactant and different intermediates (a) $CO(NH_2)_2*$, (b) $CO*$ and (c) $NH*$, for UOR on Mo-doped $Ni(OH)_2$ system with a Ni:Mo ratio of 5:1.

Table S8. The changes in electronic adsorption energy of $CO(NH_2)_2*$, $CO*$ and $NH*$ on Mo-doped $Ni(OH)_2$ system with a Ni:Mo ratio of 5:1.

Adsorbed Species	Electronic Adsorption Energy (eV)
CON_2H_4*	-0.59
CO*	0.64
NH*	0.89

Supplementary References

S1. A. Sahasrabudhe, H. Dixit, R. Majee, and S. Bhattacharyya, *Nat. Commun.,* 2018, **9,** 2014.

S2. J. Zhang, T. Wang, P. Liu, Z. Liao, S. Liu, X. Zhuang, M. Chen, E. Zschech, and X. Feng, *Nat. Commun.,* 2017, **8**, 15347.

S3. Y. Chen, Y. Zhang, X. Zhang, T. Tang, H. Luo, S. Niu, Z. Dai, L. Wan and J. Hu, *Adv. Mater.,* 2017, **29**, 1703311.

S4. S. Zhao, J. Huang, Y. Liu, J. Shen, H. Wang, X. Yang, Y. Zhu and C. Li, *J. Mater. Chem. A,* 2017, **5**, 4207-4214.

S5. M. Gao, C. Yang, Q. Zhang, J. Zeng, X. Li, Y. Hua, C. Xu, and P. Dong, *J. Mater. Chem. A*, 2017, **5**, 5797-5805.

S6. Y. Jin, X. Yue, C. Shu, S. Huang, and P. Shen, *J Mater. Chem. A,* 2017, **5**, 2508-2513.

S7. Y. Wang, G. Zhang, W. Xu, P. Wan, Z. Lu, Y. Li, and X. Sun, *ChemElectroChem,* 2014, **1**, 1089.

S8. D. Rodene, E. Eladgham, R. Gupta, I. Arachchige, and V. Tallapally, *ACS Appl. Energy Mater.,* 2019, **2**, 7112-7120.

S9. Y. Zhou, M. Luo, W. Zhang, Z. Zhang, X. Meng, X. Shen, H. Liu, M. Zhou, and X. Zeng, *ACS Appl. Mater. Interfaces,* 2019, **11**, 21998-22004.

S10. Q. Zhang, P. Li, D. Zhou, Z. Chang, Y. Kuang, X. Sun, *Small* 2017, **13**, 1701648.

S11. J. Tian, N. Cheng, Q. Liu, X. Sun, Y. He, and A. Asiri, *J. Mater. Chem. A,* 2015, **3**, 20056-20059.

S12. J. McKone, B. Sadtler, C. Werlang, N. Lewis, and H. Gray, *ACS Catal.,* 2013, **3**, 166-169.

S13. H. Tan, B. Tang, Y. Lu, Q. Ji, L. Lv, H. Duan, N. Li, Y. Wang, S. Feng and Z. Li, *Nat. Commun.,* **2022**, *13*, 2024.

S14. A. Kumar, X. Liu, J. Lee, B. Debnath, A. Jadhav, X. Shao, V. Bui, Y. Hwang, Y. Liu and M. Kim, *Energy Environ. Sci.,* 2021, **14**, 6494-6505.

S15. A. Kumar, V. Q. Bui, J. Lee, A. R. Jadhav, Y. Hwang, M. G. Kim, Y. Kawazoe and H. Lee, *ACS Energy Lett.*, 2021, **6**, 354-363.

S16. J. Mahmood, M. A. R. Anjum, S.-H. Shin, I. Ahmad, H.-J. Noh, S.-J. Kim, H. Y. Jeong, J. S. Lee and J.-B. Baek, *Adv. Mater.,* 2018, **30**, 1805606.

S17. F. Yu, H. Zhou, Y. Huang, J. Sun, F. Qin, J. Bao, W. A. Goddard, S. Chen and Z. Ren, *Nat. Commun.,* 2018, **9**, 2551.

S18. B. Weng, C. Grice, W. Meng, L. Guan, F. Xu, Y. Yu, C. Wang, D. Zhao and Y. Yan, *ACS Energy Lett.,* 2018, **3,** 1434-1442.

S19. J. Mao, C. He, J. Pei, W. Chen, D. He, Y. He, Z. Zhuang, C. Chen, Q. Peng and D. Wang, *Nat. Commun.,* 2018, **9**, 4958.

S20. R. Majee, A. Kumar, T. Das, S. Chakraborty and S. Bhattacharyya, *Angew. Chem. Int. Ed.,* **2020**, *59*, 2881.

S21. Y. Ito, T. Ohto, D. Hojo, M. Wakisaka, Y. Nagata, L. Chen, K. Hu, M. Izumi, J. Fujita and T. Adschiri, *ACS Catal.*, 2018, **8**, 3579-3586.

S22. J. Park, H. Kim, G. Han, J. Kim, S. Yoo, H. Kim and S. Ahn, *J. Mat. Chem. A,* 2021, **9**, 3677-3684.

S23. Z. Chang, L. Zhu, J. Zhao, P. Chen, D. Chen and H. Gao, *Int. J. Hydrog. Energy,* 2021, **46**, 3493.
.
S24. T. Wang, X. Wang, Y. Liu, J. Zheng and X. Li, *Nano Energy,* 2016, **22**, 111-119.

S25. F. Bao, E. Kemppainen, I. Dorbandt, R. Bors, F. Xi, R. Schlatmann, R. Krol and S. Calnan, *ChemElectroChem,* 2021, **8**, 195-208.

S26. Y. Liu, S. Liu, Y. Wang, Q. Zhang, L. Gu, S. Zhao, D. Xu, Y. Li, J. Bao and Z. Dai, *J. Am. Chem. Soc.,* 2018, **140**, 2731-2734.

S27. C. Xie, W. Chen, S. Du, D. Yan, Y. Zhang, J. Chen, B. Liu and S. Wang, *Nano Energy,* 2020, **71**, 104653.

S28. J. Dai, Y. Zhu, Y. Chen, X. Wen, M. Long, X. Wu, Z. Hu, D. Guan, X. Wang and C. Zhou, *Nat. Commun.,* 2022, **13**, 1189.

S29. A. Shan, X. Teng, Y. Zhang, P. Zhang, Y. Xu, C. Liu, H. Li, H. Ye and R. Wang, *Nano Energy,* 2022, **94**, 106913.

S30. M. Sheng, B. Jiang, B. Wu, F. Liao, X. Fan, H. Lin, Y. Li, Y. Lifshitz, S. Lee and M. Shao, *ACS Nano,* 2019, **13**, 2786-2794.

S31. T. Chao, X. Luo, W. Chen, B. Jiang, J. Ge, Y. Lin, G. Wu, X. Wang, Y. Hu and Z. Zhuang, *Angew. Chem. Int. Ed.* 2017, **129**, 16263.

S32. C. Zhu, Z. Yin, W. Lai, Y. Sun, L. Liu, X. Zhang, Y. Chen and S. L. Chou, *Adv. Energy Mater.* 2018, **8**, 1802327.

S33. F. Qin, Z. Zhao, M. K. Alam, Y. Ni, F. Robles-Hernandez, L. Yu, S. Chen, Z. Ren, Z. Wang, and J. Bao, *ACS Energy Lett*. 2018, **3**, 546-554.

S34. Y. Jia, L. Z. Zhang, G. P. Gao, H. Chen, B. Wang, J. Z. Zhou, M. T. Soo, M. Hong, X. C. Yan, G. R. Qian, J. Zou, A. J. Du and X. D. Yao, *Adv. Mater.,* 2017, **29**, 1700017.

S35. B. You, N. Jiang, M. Sheng, M. W. Bhushan and Y. Sun, *ACS Catal.*, 2016, **6**, 714-721.

S36. F. Du, L. Shi, Y. Zhang, T. Li, J. Wang, G. Wen, A. Alsaedi, T. Hayat, Y. Zhou and Z. Zou, *Appl. Catal. B Environ.,* 2019, **253**, 246-252.

S37. Y. Jin, X. Yue, C. Shu, S. Huang and P. Shen, *J Mater. Chem. A,* 2017, **5**, 2508-2513.

S38. A. Sivanantham, P. Ganesan and S. Shanmugam, *Adv. Funct. Mater*., 2016, **26**, 4661-4672.

S39. C. Du, L. Yang, F. L. Yang, G. Z. Cheng, W. Luo, *ACS Catal.*, 2017, **7**, 4131−4137.

S40. G. B. Darband, M. Aliofkhazraei, S. Hyun, A. S. Rouhaghdam and S. Shanmugam, *Nanoscale,* 2019, **11**, 16621−16634.

S41. H. Huang, C. Yu, C. Zhao, X. Han, J. Yang, Z. Liu, S. Li, M. Zhang and J. Qiu, *Nano Energy,* 2017, **34**, 472-480.

S42. Z. Yan, E. Wang, J. Gao, J. Yang, C. Wu, L. Jiang, M. Zhu and G. Sun, *ChemElectroChem,* 2017, **4**, 2190.

S43. Z. Yu, C. Lang, M. Gao, Y. Chen, Q. Fu, Y. Duan and S. Yu, *Energy Environ. Sci.,* 2018, **11**, 1890-1897.

S44. J. Zhang, T. He, M. Wang, R. Qi, Y. Yan, Z. Dong, H. Liu, H. Wang and B. Xia, *Nano Energy*, 2019, **60**, 894-902.

S45. C. Li, Y. Liu, Z. Zhuo, H. Ju, D. Li, Y. Guo, X. Wu, H. Li and T. Zhai, *Adv. Energy Mater.*, 2018, **8**, 1801775.

S46. L. Yan, Y. L. Sun, E. L. Hu, J. Q. Ning, Y. J. Zhong, Z. Y. Zhang and Y. *J.* Hu, *Colloid Interface Sci.,* 2019, **541**, 279-284.

S47. F. Li, J. Chen, D. Zhang, W.-F. Fu, Y. Chen, Z. Wen and X. J. Lv, *Chem. Commun*., 2018, **54**, 5181-5184.

S48. M. He, C. Feng, T. Liao, S. Hu, H. Wu and Z. Sun, *ACS Appl. Mater. Interfaces,* 2020, **12**, 2225-2233.

S49. Wen, X. *Int. J. Hydrog. Energy,* 2020, **45**, 14660.

S50. J. Cao, H. Li, R. Zhu, L. Ma, K. Zhou, Q. Wei and F. Luo, *J. Alloys Compd.,* 2020, **844**, 338-347.

S51. Wang, J. Wang, X. Sun, S. Wei, L. Cui, W. Yang and J. Liu, *Nano Res.,* 2018, **11**, 988-996.

S52. X. Zhang, Y. Liu, Q. Xiong, G. Liu, C. Zhao, G. Wang, Y. Zhang, H. Zhang and H. Zhao, *Electrochim. Acta,* 2017, **254**, 44-49.